Multiscale Structural and Chemical Investigations of Corrosion in CoCrMo Grain Boundaries

Alex Yu-Wei Lin

Department of Materials Science and Engineering

Northwestern University, Evanston, IL

Advisors

Laurence D. Marks

Emily E. Hoffman

Submitted in partial fulfillment of the requirements for the degree of

Bachelor of Science in Materials Science and Engineering

March 15, 2016

Abstract

Total hip replacement surgery is currently one of the fastest growing medical procedures in the United States and around the world. The permanent nature and long lifetimes of hip replacements require materials with excellent mechanical properties and biocompatibility. Cobalt-chromium-molybdenum (CoCrMo) alloys with the addition of carbon were previously determined to be suitable for hip replacements. However, this material is susceptible to corrosion due to tribological events such as joint movements and their constant exposure to corrosive body fluids. These degradation processes, which release nanoscale metallic debris particles and toxic ions into the body, do not only pose health complications but also reduce the lifetime of implants. Since there is currently a large number of patients with CoCrMo implants installed, it is critical to gain a fundamental understanding of corrosion in CoCrMo alloys, which would in turn improve their applications.

In this work, electrochemically corroded CoCrMo alloy samples were analyzed from the millimeter to nanometer scale in order to understand how different grain boundary properties impact the *in vivo* performance of the alloy. This was achieved by correlating coincidence site lattice geometry and chemical composition to localized corrosion properties. Using high-resolution transmission electron microscopy and energy dispersive X-ray spectroscopy, it is shown that higher magnitudes of chromium depletion and larger carbide precipitates are observed with increasing grain boundary interfacial energy. Additionally, the microscale morphology of corrosion crevices reveals that crevice corrosion had occurred at the crevices initiated by grain boundary sensitization. The conclusions presented can help refine the processing procedures in order to engineer higher performance CoCrMo alloys for biomedical applications.

Acknowledgements

First and foremost, I would like to thank my thesis advisor, Professor Laurence D. Marks for the opportunity to participate in academic research. Since then, his continued support and guidance for my work has been an inspiration to me. This research project would not have been possible without the education and insights he provided. I am also indebted to Emily Hoffman, a graduate student in the Marks group for her mentorship. Whether it is teaching me how to tame the FIB or helping me align the microscope, she is always willing to help. I would also like to thank Dr. Kathleen Stair for reviewing much of this work and always providing helpful advice for making complex research topics accessible for a general audience.

I would also like to thank the past and present members of the Marks group: Dr. Yifeng Liao, for patiently explaining some of the basics of tribocorrosion to me; Dr. Ahmet Gulec, Dr. Xiaoxiang Yu, Betty Peng, Pratik Koirala, Lawrence Crosby, Tassie Andersen, Lizzie Steele, and Say Young Cook for many helpful, interesting, and fun discussions regarding my project and beyond. These individuals have not only shared their own tips and tricks, but also taught me a fair amount of science and microscopy.

Last but not least, I would like to extend my deepest gratitude to my family and friends who accompanied me through the ups and downs all these years. Without their continued support and encouragement, I would not have been able to make it this far. Thank you for having faith in me.

This work was funded by the National Science Foundation on grant number CMMI-1030703. The study resulting in this report was assisted by a grant from the Undergraduate Research Grant Program which is administered by Northwestern University's Office of Undergraduate Research.

Contents

Acronyms

ADF	annular dark field.
BF	bright field.
CSL	coincident site lattice.
DF	dark field.
EBSD	electron backscatter diffraction.
EDS	energy-dispersive X-ray spectroscopy.
FIB	focused ion beam.
HAADF	high-angle annular dark field.
OIM	orientational image mapping.
SEM	scanning electron microscopy.
STEM	scanning transmission electron microscopy.
TED	transmission electron diffraction.
TEM	transmission electron microscopy.

1 Introduction

Prosthetic orthopedic implants at the hips and knees are some of the most successful procedures for patients with severe osteoarthritis and rheumatoid arthritis. Currently, more than 300,000 total hip replacement operations are performed annually in the United States (1), and this number is predicted to reach 1,800,000 by 2050 (2). The components of current artificial hip replacements on the market include ultrahigh-molecular-weight polyethylene, CoCrMo alloys, and ceramics. Metal-on-polyethylene (MoP) devices, which contain a CoCrMo femoral ball and a polyethylene cup, dominate the total hip replacement market as they have shown overall good clinical results with relatively low wear rate and long life expectancy. However, MoP devices generate polyethylene wear particles which have been shown to cause bone loss near the implant (3).

CoCrMo metal-on-metal (MoM) bearings have attracted great interest as an alternative to MoP implants because of their excellent mechanical properties, superior wear and corrosion resistance, longer service duration, and reduced inflammation resulting from such devices. MoM devices have functioned well *in vivo* and some last more than twenty years (4). At the peak of their popularity in the mid-2000s, approximately 35% of the hip replacements in the US were MoM implants based on CoCrMo alloys with the addition of carbon to harden the alloy (5). The corrosion rate *in vivo* at several microns per year is significantly lower than the value observed in MoP devices (6, 7). Despite its superior performance, MoM hip implants are not immune to biocompatibility issues caused by corrosion. The corrosion debris particles range from tens to hundreds of nanometers in size. Thus, even though the overall corrosion rate is low, adverse side effects remain unavoidable.

Cogent evidence has shown that wear debris and metal ions are released to the surrounding tissue and bone as well as other locations in the body. Elevated concentrations of cobalt and chromium ions have been detected in the blood of patients with CoCrMo implants (8, 9). Furthermore, discolored periprosthetic tissue is frequently observed during revision surgeries or post-mortem examinations. However, in light of the recent reported biocompatibility issues, there remains a large number of patients who still have these implants *in situ*. With precise heat treatments to modify their microstructures, CoCrMo alloys have the potential to be an effective material for biomedical materials and other application, which illustrates the need to analyze these alloys on the micro- and nanoscale in order to comprehend their corrosion properties.

The processes governing the degradation of these implants are unquestionably complex. It has been shown that the overall corrosion performance improves after annealing of CoCrMo alloys as segregated second phase precipitates diffuse from grain boundaries into the matrix. Additionally, annealing also introduces coincident site lattice (CSL) grain boundaries, which generally have enhanced corrosion resistance. However, it is evident that corrosion remains problematic, especially at finer length scales. At the microscale, corrosion crevices at grain boundaries are observed. At the nanoscale, chromium depleted zones form around the grain boundaries, causing the localized area to be more susceptible to corrosion attack. With these observations in mind, new insights into the corrosion mechanisms at localized regions near the surface and grain boundaries of CoCrMo alloys are developed in this work.

The aim of this study is to improve the corrosion resistance of CoCrMo alloys by identifying and understanding corrosion mechanisms through structural and chemical analyses across multiple length scales. The conclusions of this work may result in more precisely engineered and better-performing alloys for future uses, including orthopedic implants. In the present work, we study an annealed and electrochemically corroded CoCrMo alloy with various imaging methods such as white light interferometry, scanning electron microscopy (SEM), transmission electron microscopy (TEM), and scanning transmission electron microscopy (STEM). Diffraction techniques such as electron backscatter diffraction (EBSD) and transmission electron diffraction (TED) are essential for examining the crystallographic orientation of a material and its defects. Direct measurements of the chemical compositions of nanoscale chromium depleted zones and carbide precipitates are performed with high-resolution energy-dispersive X-ray spectroscopy (EDS) with STEM. Included in this introduction is a brief overview of grain boundary structure and CSLs. Experimental procedures and characterization methodology will be discussed in detail in Chapter 2, and the experimental results obtained in this work will be presented in Chapter 3. Possible corrosion mechanisms which may provide additional insights for improving corrosion properties will also be covered in Chapter 3. Lastly, this thesis concludes with a summary and suggestions for future work in Chapter 4.

1.1 Grain Boundary Structure

Grain boundaries are commonly susceptible to corrosion attack because they have low interfacial energies as well as different lattice structure and chemistry compared to grain interiors (10). These differences, which can sometimes be very small, can establish a preferred intergranu-

lar corrosion crack path along grain boundaries within an alloy. The variations of grain boundary structure, orientation, and its corresponding interfacial energy have been widely known to be significant factors that affect intergranular corrosion (11, 12). In general, grain boundary structure is quantified using the CSL model, where grain boundaries can be classified as having repeating coincident lattice points along the boundary. The degree of coincidence can be described by a Σ value, which is the ratio of coincident lattice sites to the two-dimensional crystal unit cell area. $\Sigma 3$ twin boundaries, which have very low interfacial energy, are immune to corrosion attack. On the other hand, general high-angle grain boundaries or boundaries with a low degree of lattice coincidence will be susceptible to corrosion (13, 14).

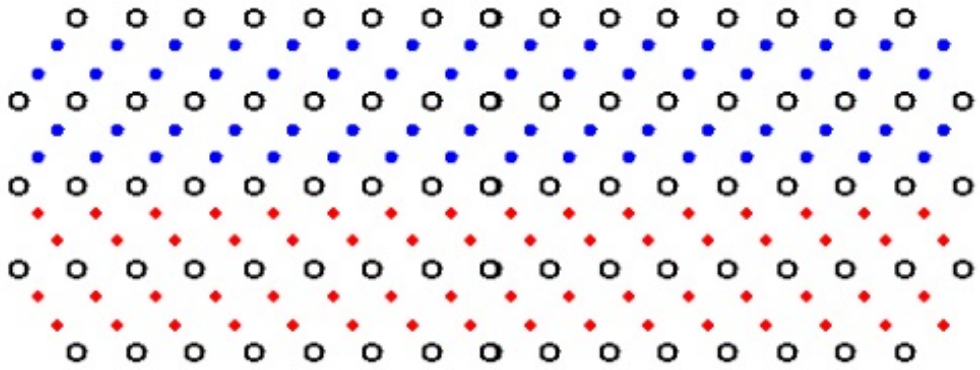

Figure 1: One of the most commonly observed CSL grain boundary is the $\Sigma 3$ twin boundary. Crystal lattices of two different grains, depicted in blue and red, share a fraction of sites on either side of the boundary.

The CSL model is an adequate tool to predict how grain boundaries will behave. There is mounting experimental evidence that shows low interfacial energy values at interfaces with a large density of coincident lattice points. However, the relationship between grain boundary interfacial energies and corrosion susceptibility remains unclear as there is still no complete quantitative model that can predict how CoCrMo grain boundary corrosion varies with grain boundary structure and the corresponding interfacial energy. Alternatively, boundary orientation and its contribution to corrosion has been well-studied for steels and nickel-based alloys. Similar experimental methods can be extended to investigating CoCrMo alloys.

Scanning electron microscopy (SEM) combined with electron backscatter diffraction (EBSD) has been the standard technique for determining grain boundary orientation and the distribution of CSL boundaries within the bulk alloys. Such experiments report results that support that low-Σ CSL boundaries are more resistant to corrosion attack and general boundaries are more

susceptible to corrosion. Lin *et al.* has shown that increasing the frequency of special CSL grain boundaries ($\Sigma \leqslant 29$) in thermomechanical processed Ni-alloys decreases the bulk intergranular corrosion susceptibility of the material (15). An investigation, completed by Panigrahi *et al.* with high-carbon CoCrMo alloys at various heat treatments, also yielded similar results. Based on the grain boundaries observed, 90% of the grain boundaries with reciprocal lattice coincidence $\Sigma 11$ or lower is completely immune to the *in vitro* electrochemical corrosion process (16).

1.2 Grain Boundary Sensitization

Sensitization, as currently understood in literature, is an increase in corrosion susceptibility as a result of heat treatments. The most general use of sensitization refers to a local reduction of the concentration of a protective alloying element. For chromium-containing alloys, sensitization is used to describe a localized depletion of chromium and explain preferential intergranular corrosion. Grain boundary sensitization in CoCrMo alloys refers to the formation of chromium depleted zones near grain boundaries due to the nucleation and growth of chromium-rich carbides. The relationship between heat treatments, localized chemical compositions, and corrosion susceptibility was first studied extensively in steel and nickel alloys. Various heat treatments have shown to reduce the fraction of second phases, allowing chromium to evenly dissolve throughout the alloy matrix, and promoting the formation of a protective oxide layer. Depletion of chromium at grain boundaries is well-documented in stainless steels and Fe-Ni-Cr alloys (17). During heat treatments and annealing, these alloys form chromium carbides primarily at the grain boundaries, resulting in Cr depletion adjacent to the boundaries. Carbide precipitation forms readily at grain boundaries due to carbon segregation and heterogeneous carbide nucleation and growth supported by fast carbon diffusion. Generally, a minimum of 13 at% Cr in solid solution is required to form protective films on steels and Fe-Ni-Cr alloys in corrosive solutions (18). Thus, the depletion of Cr at grain boundaries results in sensitized zones along grain boundaries that are highly susceptible to corrosion in certain environments.

Similar to other chromium-containing steel and nickel alloys, CoCrMo is also affected by grain boundary sensitization. By combining electrochemical corrosion testing with microscale chemical analysis, Bettini *et al.* showed that the micron sized carbide precipitates at grain boundaries vary in chemical content and also in crystallographic structure (19). Additionally, it is suggested that metal dissolution occurs at carbide boundaries due to the local depletion of the alloying elements. This observation with biomedical grade CoCrMo alloys agreed with the es-

tablished steel models, demonstrating that grain boundary sensitization should be taken into consideration for CoCrMo. However, much less is known about CoCrMo alloys. Some studies have characterized the compositions of different nanoscale carbides such as Cr_6C and Mo_6C that form in addition to the commonly observed $Cr_{23}C_6$ precipitates (20), but not in relation to heat treatment or corrosion properties. Other studies have considered grain boundary geometry and heat treatments with respect to corrosion susceptibility, but not changes in chemical compositions.

2 Experimental Procedures and Techniques

The primary objective of this work is to understand the grain boundary properties of CoCrMo alloys and their impact on corrosion performance. As discussed in the earlier section, multiple processes govern the degradation of these alloys; thus, the crystallography, microstructures, chemical compositions, and corrosion properties all need to be investigated. In this study, SEM and EBSD are used to characterize surface morphology as well as the crystallographic orientations of grains. Experimental studies are extended to the nanoscale in order to observe the initial processes for corrosion, including the nucleation and growth of carbide nanoparticles, the formation of corrosion crevices, and the development of intergranular cracks. Modelling the specific parameters for corrosion initiation is critical for determining potential heat treatment modifications that can produce CoCrMo alloys with higher overall corrosion resistance.

2.1 CoCrMo Alloy

CoCrMo alloys became a popular choice for total hip replacements and other orthopedic devices because they have a superior combination of properties including high fracture toughness, ductility, biocompatibility, strength, and corrosion resistance. High-carbon CoCrMo alloys are strengthened by the hard carbide phases giving rise to the superior wear resistance exhibited by this material. Due to its prevalence in hip replacement components, a high-carbon wrought CoCrMo alloy, in accordance to ASTM F1537-08, was used in this study. The alloy composition is given in Table 1. The wrought CoCrMo alloy was annealed in an air furnace for 24 hours at 1230 ^{o}C. This heat treatment was most successful in reducing the bulk corrosion rate, localizing corrosion to grain boundaries, and optimizing the *in vivo* performance. The solution-annealed CoCrMo sample was then grinded, polished, and then electrochemically corroded according to the procedures used by Panigrahi *et al.* (21)

Table 1: High-carbon CoCrMo Alloy Composition

(at%)	Co	Cr	Mo	C	Si	Mn	Ni	Fe
ASTM F1537-08	Balance	30.3	3.6	1.14	1.34	0.73	0.17	0.14

2.2 Characterization and Theory

The characterization methods used herein examine the morphologies of CoCrMo grain boundaries from the millimeter scale to the nanometer scale. Various imaging techniques, combined with diffraction methods and chemical analysis, provide insights into how metallurgy impacts the localized corrosion behavior at grain boundaries.

2.2.1 Scanning Electron Microscopy (SEM)

Scanning electron microscopy (SEM) is one of the most versatile and popular imaging methods available for examining the microstructural features of an alloy. An important capability of SEM is its ability to resolve features on the micro- and nanoscale. In addition to its high spatial resolution, SEM also has a large depth of field, which provides images with a three-dimensional appearance, and as a result, much more information can be revealed from the specimen in comparison to optical microscopy methods. Typically, SEM is used for obtaining topographical images for microstructural analysis and basic chemical microanalysis in metal alloys.

Although SEM micrographs are generally very intuitive, the theory behind image formation is crucial for interpreting these micrographs and appreciating the versatility of the instrument. In the SEM, a fine high-energy electron beam scans across the surface of the sample and various radiation signals are produced. The interaction between the electron beam and the atoms within the sample generates secondary electrons, backscattered electrons, and characteristic X-rays. These radiation products can then be collected by a detector. For the most common imaging mode in the SEM, low-energy secondary electrons are emitted from the surface of the sample due to inelastic scattering of the electrons by the atoms in the sample. The secondary electrons are then collected by the Everhart-Thornley detector. The signal strength of the secondary electron image is dependent on the angle between the sample and detector, so the formed images are effective for characterizing the surface topography of the sample. Unlike optical microscopes or transmission electron microscopes, no real image is formed in the SEM. Alternatively, images are formed by scanning the electron beam in a raster pattern across the sample in synchronization

with the scanning beam in the cathode ray tube screen. Thus, the topographical information shown in the formed image will represent the true and exact shape of the region of interest. The fine scanning electron beam used for image formation also gives rise to the large depth of field of the instrument.

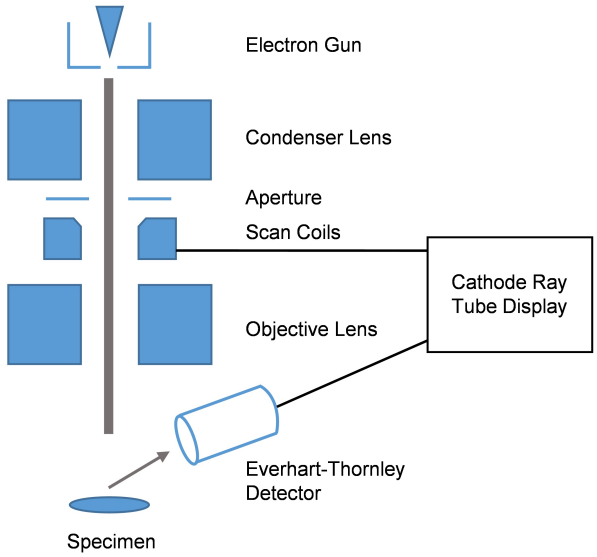

Figure 2: Schematic diagram showing the principal components of a typical scanning electron microscope.

In addition to secondary electrons, backscattered electrons and characteristic X-rays are also emitted from the sample. Backscattered electrons are produced by elastic interactions of the electron beam with the nuclei of atoms and can be used to acquire compositional information as the intensity of the signal varies with the atomic number of the scattering atoms. In other words, heavier elements with higher atomic numbers will backscatter electrons more strongly. Backscattered electron imaging will generate micrographs that show atomic number contrast. Furthermore, backscattered electrons can form backscattered electron diffraction patterns that can be used to identify the phases and crystallographic structures within the sample. Electron backscatter diffraction and its role in this work will be discussed with more detail in Section 2.2.2. Lastly, characteristic X-rays are also generated by the interaction between the specimen and the electron beam. A SEM equipped with energy dispersive X-ray spectroscopy can analyze the X-ray signals and map the distribution of the elemental constituents of various regions of interest such as microscale second-phase inclusions.

For this study, SEM characterization was performed on the FEI Quanta ESEM operating at an accelerating voltage of 30 kV. Various regions of the electrochemically corroded CoCrMo surface were imaged at 300x to 600x magnification depending on the grain sizes in the particular regions.

2.2.2 Electron Backscatter Diffraction (EBSD)

As mentioned in Section 2.2.1, backscattered electrons are generated when the electron beam interacts with atoms within the sample. These electrons, diffracted by the atomic layers in a crystalline sample, can be detected by a specialized detector and generate diffraction bands called Kikuchi lines. The EBSD detector is essentially a camera that records and digitizes the different diffraction patterns generated from the different sites within the sample. For optimal results, the detector is inserted into the SEM chamber and brought to within several millimeters from the surface of the sample. Kikuchi lines are two-dimensional projections of the lattice planes in the crystalline sample and provide the crystallographic orientation of grains. A collection of Kikuchi lines is used to form electron backscatter diffraction patterns (EBSP). Oftentimes, these EBSPs are compared to a database within a computer post-processing software that includes crystallographic information for various phases. The Kukuchi lines are then indexed and phase information and crystal orientations can then be extracted from the EBSPs.

EBSD is a relatively fast method for characterizing the crystal orientations over a large area. In this study, a typical scan surveyed an area that was approximately 250 μm by 250 μm. The crystallographic orientations of selected neighboring grains were characterized with a post-processing software in order to determine the grain boundary structure. Orientational image mapping (OIM) indicated the misorientation of the grain boundary interface and classified each boundary according to the CSL model. OIM also determined the locations of boundaries that were not previously observed in SEM imaging, such as low-angle grain boundaries, twin boundaries, and other grain boundaries that were immune to corrosion.

A FEI Quanta ESEM equipped with an Oxford EBSD detector was used to acquire and index EBSPs on the corroded CoCrMo sample surface. An accelerating voltage of 30 kV and a step size of 0.6 μm were used as these conditions provided sufficient signal and precision for OIM. The acquired Kikuchi patterns were indexed using the commercially available Oxford AZtec EBSD processing software. Using the Oxford Tango post-processing software, noise reduction was performed in order to minimize the impact of surface roughness caused by corrosion. Also, the misorientation of relevant grain boundaries was determined. The Brandon Criterion was used to

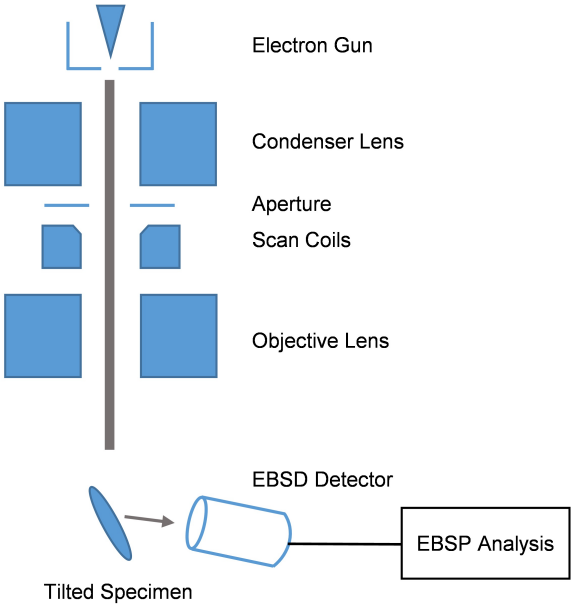

Figure 3: Schematic diagram showing the experimental configuration for EBSD OIM data acquisition.

classify the Σ, which is the ratio of coincident lattice sites to the two-dimensional crystal unit cell area, of each identified CSL grain boundary.

2.2.3 White Light Interferometry

White light interferometry, also commonly known as 3D profilometry, is a fast and non-destructive way to characterize surface topography. An interferometer is an optical device that splits a light beam from a single source and then recombines the two separate beams to create an interferogram. By analyzing this pattern, we can then determine the difference between the two optical paths. A CCD camera is used to image the interferogram and the intensity data is then digitized. In a typical 3D profilometer, an interferometer is combined with an optical microscope to allow for higher resolution and more accurate measurements. Moreover, white light interferometry is capable of characterizing rough surfaces with surface variations of up to 10 mm with a vertical resolution of approximately 3 nm. Depth measurements of corrosion pits and crevices from the electrochemically corroded CoCrMo sample can be quickly and accurately acquired via this surface characterization method. This technique was used to measure the width

of corroded grain boundaries and depth of corroded regions with respect to the surrounding surface, respectively.

A Bruker Contour GT-K 3D optical microscope equipped with a Mirau interferometer objective lens was used to quantify the surface topography of the corroded CoCrMo alloy. A magnification of 40x was used to capture the profile of the corroded surface in a 2D projection of approximately 250 μm in length and 300 μm in width. In total, 25 grain boundaries, 13 CSL boundaries and 12 non-CSL boundaries, were characterized for their depth and width. For each individual grain boundary, 15 to 20 depth and width measurements were collected. On average, a single depth measurement was acquired per 0.5-1.0 μm along the boundary. Additionally, the width of the corroded boundary was acquired by measuring the distance between the two edges of the corroded crevice at the boundary. The means of the depth and width measurements and also the range to the 95% confidence level were then computed.

2.2.4 Focused Ion Beam (FIB)

A dual-beam FEI Helios Nanolab focused ion beam (FIB) system was used to perform *in situ* lift-out of TEM lamellae from CSL grain boundaries within the annealed CoCrMo alloy. The FIB consists of a scanning electron imaging beam operating at 10 kV and 1.4 nA and a focused ion milling beam orientated at 52° to the electron beam operating at 30 kV from 9.2 nA to 48 nA. Specific CSL grain boundaries of interest were identified from the EBSD OIM data. Using the FIB system for TEM sample preparation, a cross section of the selected grain boundary was then machined into an approximately 100 nm thick, electron-transparent TEM sample for further analysis. The CoCrMo lamella sample was a cross section of the grain boundary, spanning 3-4 μm on either side of the boundary and going 4 μm deep below the bulk surface. Six asymmetrically-corroded CSL boundaries and one completely immune CSL boundary were prepared into TEM lamellae samples.

2.2.5 Transmission Electron Microscopy (TEM)

Transmission electron microscopy (TEM) is one of the most effective characterization techniques as it has the ability to form a fine probe for nanoscale characterization while simultaneously collecting crystallographic information with transmission electron diffraction (TED). TEM is particularly effective for defect analysis in polycrystalline materials; for example, grain boundaries, second phase precipitates, and dislocations can be observed. Unlike in the SEM, the electrons pass through a thin, electron-transparent specimen, and the transmitted electrons are

collected and focused onto a viewing component such as a CCD camera or a photographic film. The TEM uses a series of electromagnetic lens to accelerate the electrons and focus the electron beam onto a sample.

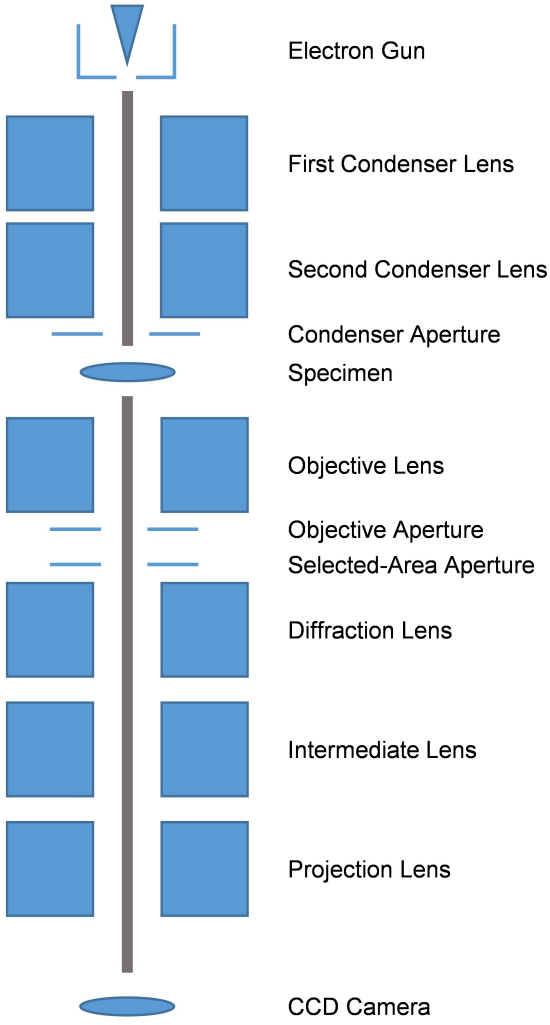

Figure 4: Schematic diagram showing the principal components of a typical transmission electron microscope.

When a high-energy electron wave interacts with the specimen, some of the incident electrons will transmit through while other electrons will be diffracted. As the electrons pass through the sample, the objective lens focus the electrons to form a diffraction pattern. At the imaging plane of the objective lens, the electrons form an image. By inserting an objective aperture at the focal

plane of the objective lens, image contrast can be increased. The various imaging planes within the TEM enable the collection of images from real space and reciprocal space.

A typical experiment in the TEM requires a combination of diffraction patterns and images and cross-referencing these results to draw definitive conclusions. As mentioned before, an electron beam is accelerated through a thin specimen and multiple diffracted beams and the transmitted beam are found at the bottom surface of the specimen. When the electrons are travelling through the sample, each atom within the sample plays a role in scattering the beam. Only for specific crystallographic directions as defined by the crystal planes are the scattered electron waves in phase. When two diffracted waves are in phase, the constructive interference of these waves will result in a strong reflected beam. From fundamental diffraction principles, the difference between the two pathlengths must be an integer multiple n of the wavelength λ for constructive interference. From crystallography, we define the pathlength difference as a function of the interplanar spacing d_{hkl} and the angle θ relative to the incident beam. This results in Bragg's law:

$$d_{hkl} \sin\theta = n\lambda \tag{1}$$

As shown, we observe strong diffracted beams when certain crystal planes are oriented at the appropriate angle relative to the incident beam. This angle is also equivalent to the angle between the diffracted and transmitted beams. Understanding electron diffraction is crucial for interpreting TEM images and the different imaging modes in the TEM.

Images are formed by the transmitted electrons and diffracted electrons. By inserting an objective aperture, the diffracted electrons exiting the sample can be filtered, thus preventing them from contributing to the image. This is how a bright field (BF) image is formed. In contrast, specific diffracted beams can be selected by the objective aperture in order to form a dark field (DF) image. Since diffraction contrast is the primary contributor for contrast in crystalline samples, BF and DF imaging are rather useful for examining microstructures and defects.

A Hitachi 8100 TEM operating at 200 kV was used for BF, DF, and TED. TEM was used to analyze the structure of CSL grain boundaries of different corrosion severity. BF imaging and TED were used to examine the presence of nanoscale carbide precipitates at these selected grain boundaries. A JEOL 2100F TEM operating at 200 kV was used for high resolution imaging of the carbide nanoparticles at the grain boundaries.

2.2.6 Scanning Transmission Electron Microscopy (STEM)

The scanning transmission electron microscopy (STEM) is a very powerful instrument capable to high-resolution imaging and nanoscale analysis. The STEM is similar to the SEM, as the electron beam is also focused by a series of lenses to form a fine electron probe at the specimen. The electron probe is scanning the sample in a raster pattern. The scattered electrons are detected by STEM detectors that are placed after sample. In the STEM, the size of the electron probe controls the spatial resolution of the instrument. Commonly, the probe sizes in modern STEMs are at the atomic scale and atomic resolution images and high-resolution elemental analysis can be readily done. However, electromagnetic lenses suffer from inherent imperfections, in particular spherical and chromatic aberrations. Aberrated electron beams will not be properly focused at the appropriate probe position, thus decreasing the spatial resolution of the microscope. In order to remedy this problem, many modern STEMs are equipped with aberration correctors that account for the aberrations within the lenses. As a result, these state-of-the-art microscopes offer superior spatial resolution.

The highest resolution images containing the most information are formed by the transmitted electrons. Similar to the conventional TEM, the STEM is capable of acquiring BF images via a BF detector. STEM also uses the annular dark field (ADF) detector, which only collects the scattered electrons over an annulus at a high angle. ADF imaging provides diffraction contrast and some sensitivity to atomic number (Z) as different elements will appear at varying intensities. To further improve the Z-contrast in images, a high-angle annular dark field (HAADF) detector can be inserted to collect the electrons that scatter by a higher angle than in ADF mode. At high-angle conditions, the elastic scattering of the atoms within the sample depends significantly on the atomic number. Additionally, diffraction contrast is suppressed and elemental composition changes can be more clearly observed with HAADF imaging.

Similar to SEM, STEM also generates characteristic X-ray signals that can be collected and analyzed in order to characterize the elemental compositions in a region of interest. Since STEM operates at a much higher accelerating voltage and the samples are thin, spatial resolution is significantly better as the electron beam is scattered less by the sample. However, the beam-specimen interaction volume is also much smaller in STEM so the X-ray count rates will be lower. At higher magnifications, samples can potentially drift. The TEM EDS processing software is capable of correcting the sample drift and stabilizing the image so the maps will not be distorted

and the features can be accurately interpreted.

A JEOL 2100F TEM operating at 200 kV in STEM mode was used for ADF imaging and EDS chemical analysis. The JEOL 2100F had a 1 nm probe size, and allowed for EDS line scans across carbide precipitates for minimal noise. EDS results from this microscope is processed through the Inca software. STEM was also performed on the JEOL ARM200CF with a windowless EDS detector to perform high-resolution EDS mapping for four selected CSL boundaries. The aberration-corrected JEOL ARM200CF provided a probe size of 0.13 nm. The maps were collected from an area, roughly 300 nm by 300 nm, that encompassed the grain boundary and carbides. EDS maps were acquired for approximately 15 minutes from each area of interest in order to acquire sufficient signal for high-resolution chemical analysis. The acquired EDS maps were analyzed using the Oxford AZtec TEM processing software. Only Co, Cr, and Mo concentrations were considered in the chemical quantification as other minor alloying constituents demonstrated very little or no change across various features within the characterized area.

3 Results and Discussion

3.1 Corrosion in Coincident Site Lattice Boundaries

Grain boundaries are fundamental planar defects within polycrystalline materials and their properties can largely impact a material's bulk mechanical properties. Certain special orientations between two neighboring grains result in coinciding lattice points at grain boundaries. It is generally understood that these geometrically special CSL grain boundaries have enhanced mechanical properties due to the small grain boundary interfacial energies associated with these interfaces. In CoCrMo alloys, we observe preferential corrosion of varying degrees of severity in different grain boundaries (Figure 5). From general observations, highly-ordered twin boundaries with low interfacial energies are completely immune from corrosion attack; while, high-energy grain boundaries with fewer coincident lattice points are more susceptible to corrosion. How-

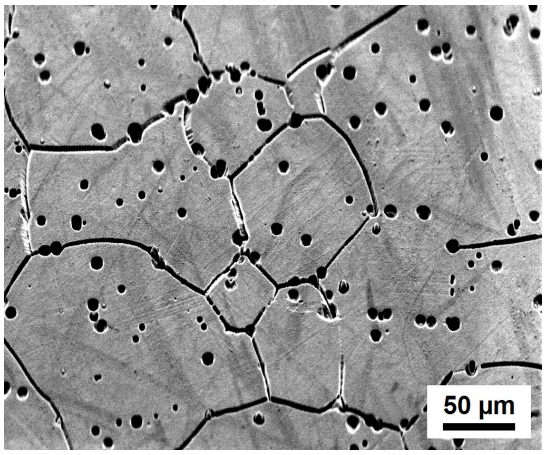

Figure 5: Preferential corrosion with varying degrees of corrosion severity in a CoCrMo alloy.

ever, the grain boundary interfacial energies do not monotonously increase with the degree of lattice coincidence, designated by Σ. Additionally, certain CSL boundaries are partially or asymmetrically corroded, suggesting that these orientations are more resistant to corrosion attack in comparison to general high-angle grain boundaries. Further studies in CSL grain boundaries are necessary to elucidate the role of grain boundary structure on the corrosion susceptibility, and ultimately, the performance of CoCrMo alloys.

3.2 Coincident Site Lattice (CSL) Model

3.2.1 Previous Studies

The effect of grain boundary misorientation on the intergranular corrosion behavior has been studied previously in steels and Ni-Cr alloys by determining if low-angle grain boundaries or CSL grain boundaries are more corrosion resistant than randomly-oriented high-angle grain boundaries. As first proposed by Watanabe (21), grain boundary engineering increases the proportions of low-energy CSL grain boundaries in order to enhance the strength and ductility of metal alloys. One of the early successes of grain boundary engineering is shown in high-performance Ni-Cr alloys as increasing the frequency of low-Σ grain boundaries with thermomechanical processing decreased the bulk intergranular corrosion susceptibility of the material (15). There are several ways to alter the grain boundary character distribution and produce a microstructure with improved properties, of which twinning-related grain boundary engineering is the most well-known. Σ3-related CSL grain boundaries generate other low-Σ boundaries and consequently, disrupts the interconnected random grain boundary network.

As observed in Ni-Cr alloys (15, 22) and steels (23), the proportion of CSL grain boundaries and also the resistance to intergranular corrosion increased by raising the proportion of the Σ3-related CSL grain boundaries via various thermomechanical treatments. Similar observations have been made in CoCrMo alloys. Annealing has been shown to shift the grain boundary character distribution by increasing the number of CSL boundaries. Furthermore, various annealing temperatures and times have been tested by observing the roughness of the surface after electrochemical corrosion.

Low-Σ grain boundaries have low corresponding interfacial energies due to the small distortions of atomic bonds, resulting in small free volumes. With this understanding, it is also pertinent to study the effect of CSL grain boundaries on grain boundary sensitization, notably the nucleation and growth of carbide precipitates. The influence of grain boundary structure on

sensitization and subsequent intergranular corrosion was studied by Palumbo *et al.* for nickel alloys (24). Geometrically-special CSL boundaries have been found to inhibit the depletion of soluble Cr in the vicinity of the grain boundary and therefore resist the sensitized condition for enhanced corrosion resistance (15). The size and spacing of the intergranular $M_{23}C_6$ carbides were dependent upon the characteristics of the grain boundary. Smaller carbides were found at $\Sigma 3$-related CSL grain boundaries, and larger carbides were found at $\Sigma 7$ and $\Sigma 21$ boundaries, suggesting that their energies were not appreciably lower than those of randomly oriented boundaries (25). Furthermore, crystalline defects have been shown to affect the formation of chromium carbides. Grain boundaries with intrinsic dislocations along the boundaries acted as sinks for solutes, allowing chromium carbides to readily form, thus altering the chemistry of the surface oxide. Intergranular boundary defects were shown to serve as preferential sites for passivation film depletion and with increasing sensitization; as a result, the potential required for initiation corrosion at these sites was reduced (24).

It is known that heat treatments, carbide size and location, and grain boundaries are all factors in formation of the protective chromium oxide film, and therefore dictate the corrosion resistance of a metal. The sensitization was often demonstrated through accelerated corrosion testing, and then measured through electrochemical potentiokinetic tests and visual analysis of the corroded surface (26, 27). By observing corroded grain boundaries and microscale carbides with severe corrosion around them with light microscopy or SEM, a metal was concluded to be sensitized. The observed corresponding chromium depletion zones were tens to hundreds of microns in size. Assessment of grain boundary sensitization and carbide precipitation behavior on different grain boundary orientations, completed mostly in steels, did not use advanced characterization methods for chemical analysis.

3.2.2 Limitations

A noted issue with the CSL model is that the distribution of coincident lattice points is anisotropic. It is necessary to consider grain boundary plane orientation before accounting for deviations from CSL orientations. For example, certain sections of a $\Sigma 25$ CSL boundary may have a higher density of coincident lattice sites than other sections of much lower CSLs (28). It is also possible that boundaries of the same Σ have different distributions of coincident lattice points, resulting in different interfacial energies. This makes classifying the corrosion susceptibility exclusively with the geometrical parameters of CSL grain boundaries imprecise and problematic.

One of the limitations of the CSL model is that there are different sets of criteria used to classify whether a grain boundary is a CSL boundary or not. The Brandon criterion (29):

$$\Delta\theta_{max} = 15^{o}\Sigma^{-1/2} \tag{2}$$

is one of the most commonly used criterion to categorize individual boundaries based on crystallographic parameters, especially in automated orientation mapping with EBSD. This simple formula accounts the maximum deviation from exact coincidence conditions (measured in degrees) for a specific CSL match and consequently separates 'special' grain boundaries from general grain boundaries. The more restrictive Palumbo-Aust criterion:

$$\Delta\theta_{max} = 15^{o}\Sigma^{-5/6} \tag{3}$$

is supported by experimental evidence such as transmission electron microscopy (TEM) studies and electrochemical etching experiments that pertain to the corrosion and cracking susceptibility of several metals and alloys. Approximately 97% of the low-Σ grain boundaries classified using the Palumbo-Aust criterion were found to demonstrate 'special' corrosion-resistant behavior (24).

In literature, the CSL model is the most commonly invoked for classifying different grain boundary structures. However, the effects of CSLs on corrosion properties have large variations across multiple studies. Several studies indicate that CSL grain boundaries are extremely resistant to intergranular corrosion and that a material can be engineered to be more corrosion resistant by creating a network of these geometrically-special CSL boundaries (30, 24). In contrast, other studies have concluded that almost all CSL boundaries are prone to corrosion cracking and that the Σ parameter is inadequate to determine the susceptibility of grain boundary corrosion (31). Some studies find a correlation between grain boundary energy and intergranular corrosion properties (12, 32). However, such relationships are not always consistent. Consequently, variations in grain boundary energy with misorientation angle cannot be used exclusively to predict all of the grain boundary properties necessary to model intergranular corrosion.

The varying rigor of the classification criterion also led to many different interpretations regarding the validity of CSL models. Experimental work conducted by Gertsman and Bruemmer have found that most CSL boundaries, with the exception of $\Sigma 3$ twin boundaries, are susceptible to varying degrees of intergranular corrosion cracking (31). They concluded that other chemical factors such as precipitation and segregation at grain boundaries, in addition to the geometrical parameters of grain boundaries, are necessary to determine corrosion susceptibility. Despite its

prevalent use across grain boundary research, the link between the Σ parameter and the physical properties of the boundary has been questioned in a few studies (33, 34).

3.2.3 Experimental Results

From SEM imaging and EBSD analysis, it was abundantly clear that preferential intergranular corrosion had occurred (Figure 6-7). All of the identified twin boundaries were immune to corrosion attack, while corrosion crevices of various sizes formed at certain CSL boundaries. Almost all general high-angle grain boundaries and high-Σ CSL boundaries were corroded. EBSD scans and 3D profilometry show that there was some relation between the corrosion depth of grain boundaries and their geometry given by the degree of lattice coincidence. 57 out of the 96

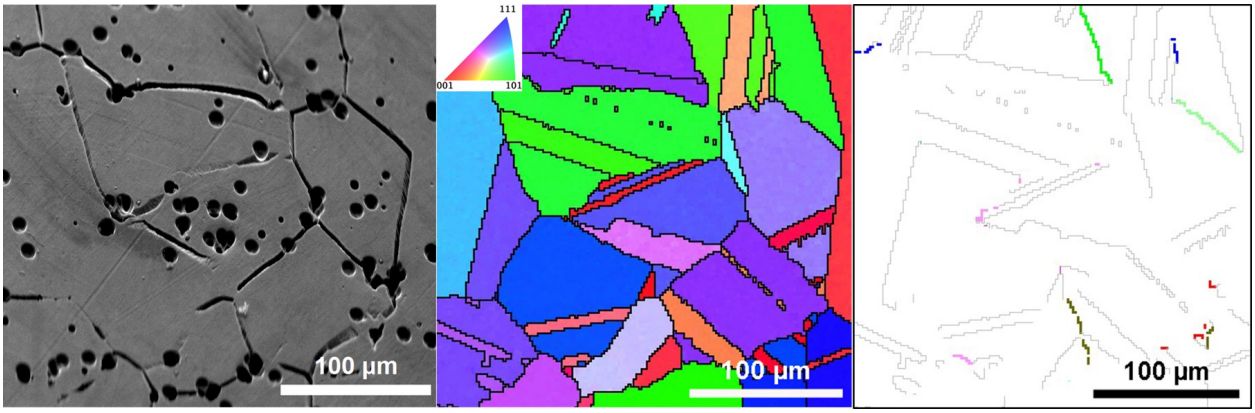

Figure 6: Individual grains were mapped using their crystallographic orientation and CSL grain boundaries can be identified from the crystallographic data.

non-twin CSL grain boundaries examined exhibited some form of corrosion resistance and 31 of these grain boundaries are above Σ11, which has been previously determined as a threshold for corrosion resistance (5). In addition, it has been determined that 100% of grain boundaries below Σ11 did not corroded more than 0.60 µm in depth. Beyond Σ35, corrosion depths of greater than 1.0 µm were observed.

These results agreed with our previous understanding of corrosion susceptibility in CSLs, as low-Σ grain boundaries with low interfacial energies were resistant to corrosion, and high-Σ boundaries with higher energies were severely corroded. However, grain boundary interfacial energies do not necessarily monotonically increase with Σ as shown by certain CSL boundaries such as Σ17 and Σ25 boundaries did not fit into the predictive model. This suggested that grain boundary interfacial energies could be used to approximate but not adequately explain corrosion susceptibility in CoCrMo alloys.

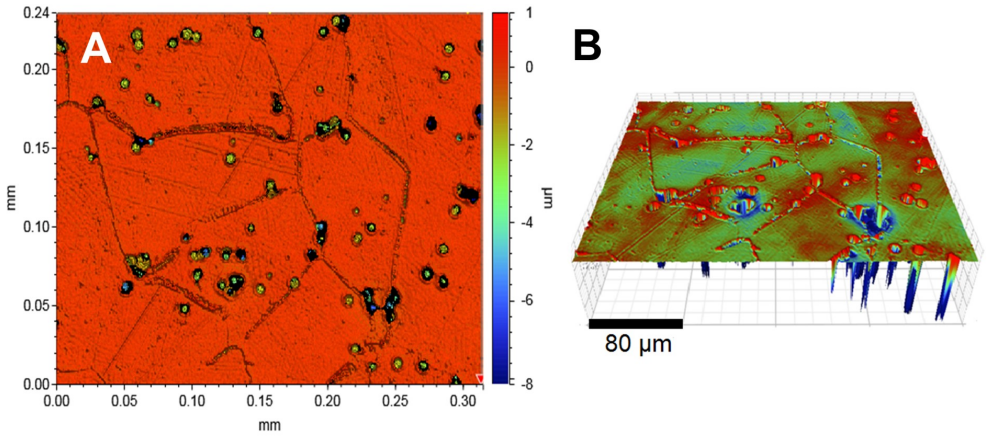

Figure 7: (A) 3D measurements of the surface profile are mapped and used to determine corrosion severity. (B) A 3D reconstruction of the sample area via the 3D profilometry data.

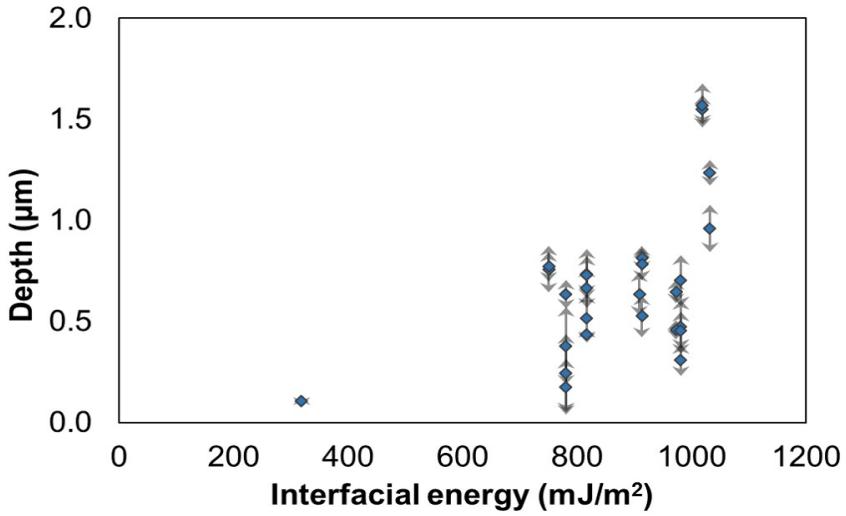

Figure 8: Interfacial energies associated with different lattice configurations in CSL grain boundaries could be used to estimate corrosion susceptibility.

In order to estimate the interfacial energies of CoCrMo CSL grain boundaries, molecular dynamics calculations for face-centered cubic (fcc) CSL grain boundaries in pure aluminum, nickel, and copper were used (35). Since CoCrMo alloys have a metastable fcc matrix, a scaling factor, determined from the calculated solid state surface energies of the main alloying elements, was applied. The corrosion depth plotted with respect to the grain boundary interfacial energies of CSL boundaries confirmed that higher energy boundaries with lower lattice coincidence were

more susceptible to corrosion (Figure 8).

3.3 Grain-Boundary Assisted Corrosion

As mentioned in the introduction, grain boundary sensitization occurs in CoCrMo alloys with the nucleation and growth of carbide precipitates and the localized chromium depletion near the boundaries. Contrary to observations from steels and Ni-Cr alloys, the chromium depleted zones were much smaller and less intense in the annealed CoCrMo alloy. Initial TEM imaging of corroded CSL grain boundaries revealed faceting caused by the second phase carbides, with these sensitized boundaries appearing wavy and irregular (Figure 9). In contrast, boundaries immune to corrosion were clean with very small or no carbides. These interfaces were also almost completely straight (Figure 10). For all six

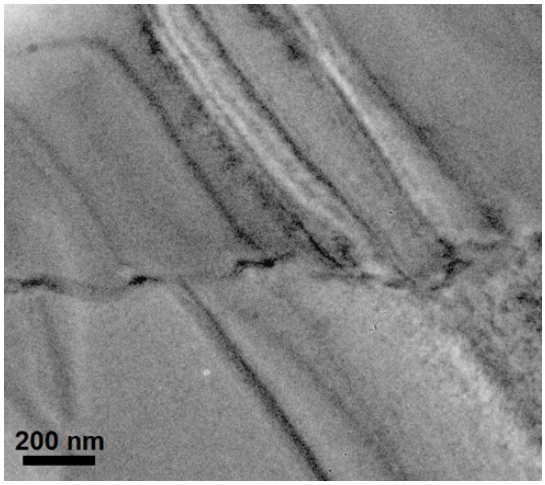

Figure 9: BF TEM showed that the corroded Σ13 grain boundary was faceted by carbides.

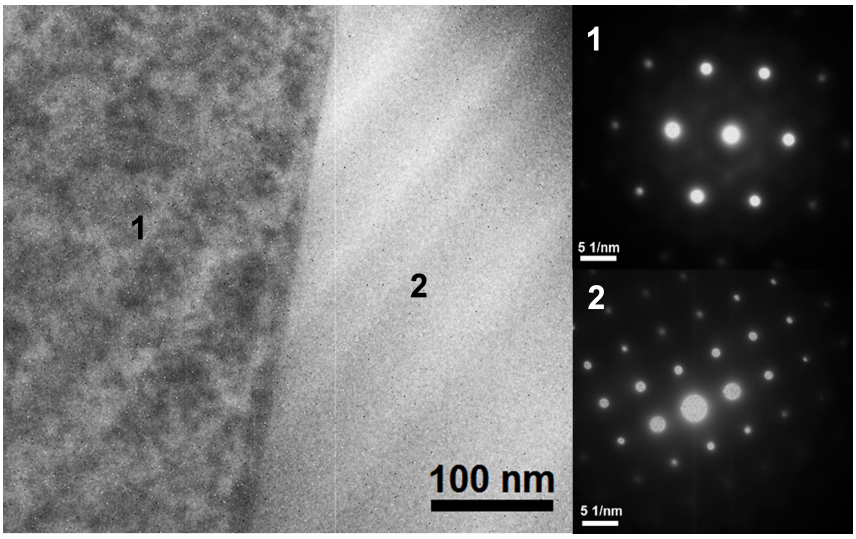

Figure 10: The immune Σ17 grain boundary was straight without deviations and did not show carbides. TED patterns of the two neighboring grains confirmed the presence of a grain boundary.

partially corroded boundaries, chromium carbides were dotted along the grain boundaries. From

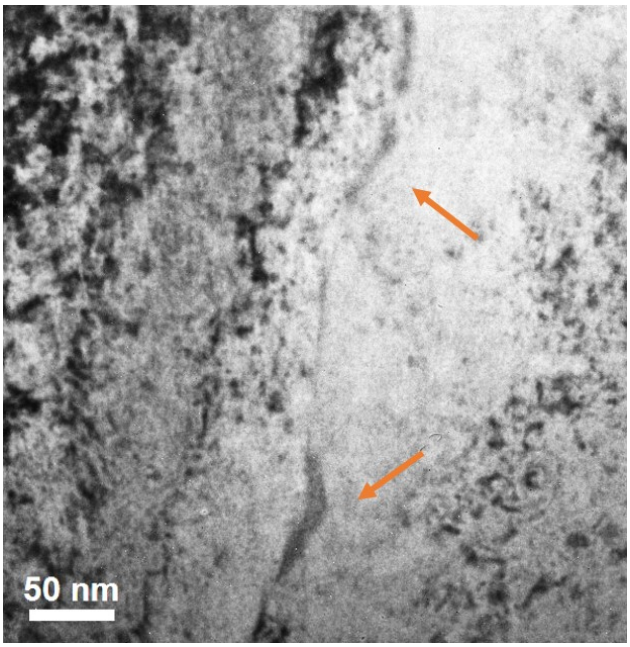

Figure 11: BF TEM image of lens shaped carbides (indicated by arrows) at a partially corroded Σ25 grain boundary.

BF TEM images, nanoscale carbide precipitates of approximately 50-100 nm in length and 10-20 nm in width were observed (Figure 11). Moreover, the chromium carbides were lens shaped, and were aligned epitaxially with the grain on the concave side of the carbides.

HAADF imaging combined with high-resolution EDS mapping revealed the different carbide morphologies. Most carbides had the same lens shape as previously observed in BF TEM; however, selected lower energy CSL boundaries contained thin and plate-like carbides. This suggested that the grain boundary structure had some control over the morphology of the carbide precipitates, but the exact mechanisms behind this have yet to be studied. A representative high-resolution EDS map shows the lens shaped chromium carbide at the grain boundary of the CoCrMo alloy (Figure 12). The clearest EDS signals showed the primary elements of the alloy, Co, Cr, and Mo as maps and with a quantized chart from key regions in Table 2. The area around the carbide contained a chromium depletion zone where the chromium composition was reduced around the carbide and along the grain.

For another carbide map in Figure 13, we observed a Cr-depleted zone along the grain boundary in between the two carbides. The three carbides were of ~50 nm and the depleted zone was seen for ~10 nm on either side of the carbide. For the four samples examined in high-resolution EDS scans were taken along 2-5 carbides of each sample, the carbide composition, matrix com-

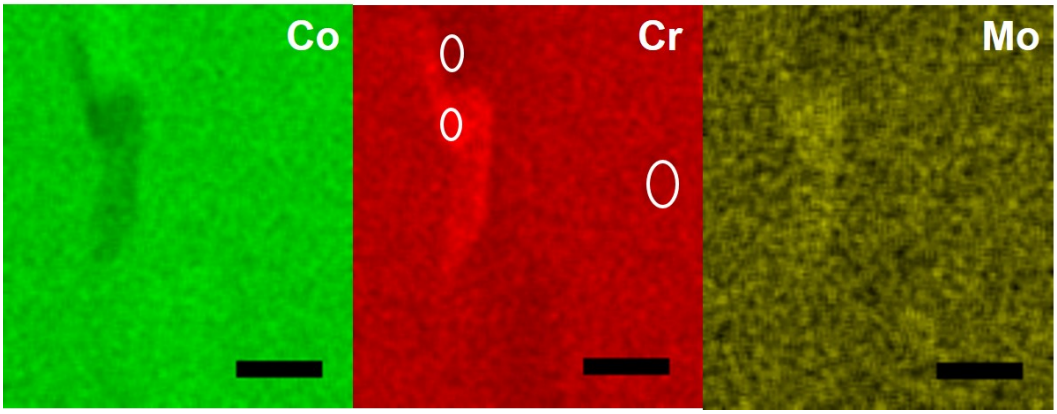

Figure 12: The chromium-depleted zones surrounding carbides are quantified with EDS mapping. Spectra were acquired at the sites represented by the circles. Scale bars are 50 nm.

Table 2: EDS quantification of key regions in Figure 12

(at%)	Co	Cr	Mo
Matrix	63.5	32.0	4.5
Carbide	48.1	46.0	5.9
Cr-depleted zone	69.9	27.3	2.8

position, and depleted zone compositions were quantified from the respective spectra.

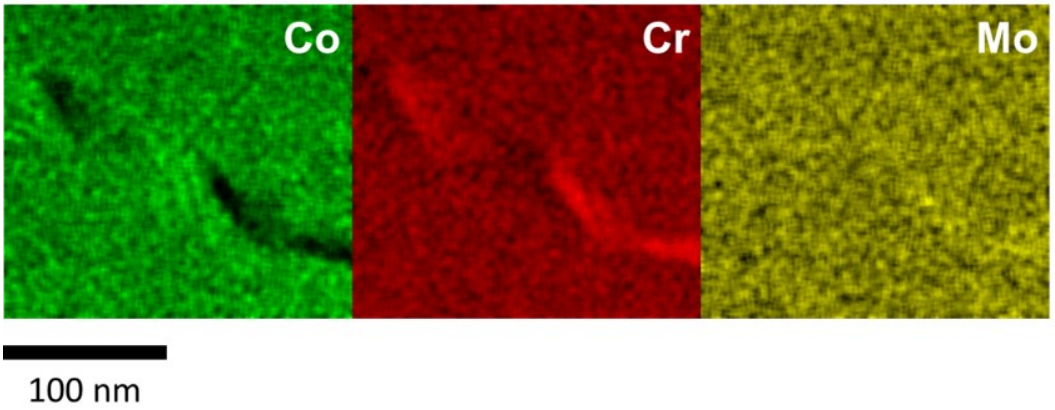

Figure 13: High-resolution EDS mapping was also able to show the chromium-depleted regions between two chromium carbides and ~10 nm from the carbides.

At the second Σ25 boundary observed in the data set, a change in carbide morphology was observed. Instead of the conventional lens shape, the carbides appeared thin and plate-like

(Figure 14). Although some observed carbides at this boundary reached 100 nm in length, the maximum widths were only 10 nm. Furthermore, EDS mapping indicated that the chromium depletion was only 2 at% about 2.5 at% less depletion when compared to the Σ13 boundary . Interestingly, the carbides were aligned in the same direction, suggesting that there was a preferential growth direction. This Σ25 boundary had a smaller corrosion depth in comparison to the aforementioned Σ13 boundary and also other Σ25 boundaries. It can be inferred that there was a slightly smaller interfacial energy, which altered the sizes of the carbide precipitates as well as the amounts of Cr depletion.

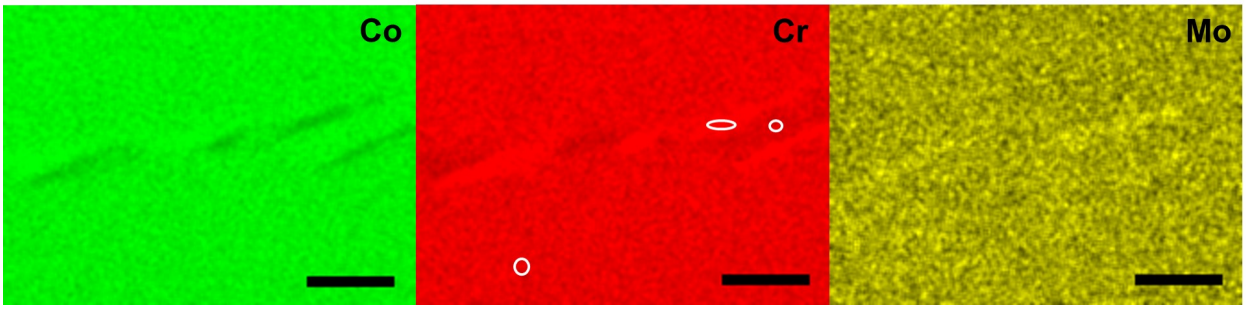

Figure 14: Flat plate-like carbides observed in EDS maps of a Σ25 boundary. Scale bares at 100 nm.

Table 3: EDS quantification of key regions in Figure 14

(at%)	Co	Cr	Mo
Matrix	66.8	31.1	2.1
Carbide	54.3	42.6	3.1
Cr-depleted zone	68.4	29.4	2.2

For the Σ17 sample with carbides smaller than 50 nm, the chromium depletion, which was the difference between the matrix chromium composition and the chromium composition along the grain boundary, was approximately 1.5 at%Ṫhe size of carbide hit a threshold where a true chromium depleted zone was not able to form, and left that grain boundary immune to corrosion attack.

3.4 Crevice Corrosion

The compositional depletion and the energy gain from removing the boundary provides the driving force for the initial attack at the grain boundary, but this does not fully explain the

experimental data. The dissolution rates for crevices and pits have been long linked to kinetic Wulff models that show the shape of a corrosion crevice is dependent on individual dissolution rates along various directions (36). In our alloy, we have the dissolution rate down the boundary which affects the depth, and the dissolution rate normal to the boundary which affects the width. If the local energy terms caused by sensitization were the only driving force, the attack would be straight down the boundary and approximately as wide as the width of the chromium depletion zone. This, however, was not the case. The width of the attack was orders of magnitude larger than the measured depletion zone. Hence, once attack has initiated at the boundary a second mechanism has to take over the dissolution process.

During crevice corrosion, oxygen diffusion is restricted by the small crevice opening. The limited concentration of oxygen causes an anodic imbalance as the cathodic reactions in the crevice are inhibited. Cathodic reactions at the bulk surface can continuously maintain the anodic reactions in the crevice through the transport of electrons and ions. Under these conditions, metal dissolution occurs readily and metal ions are released as a result. Hydrolysis of the metal ions will reduce the pH of the crevice solution, creating a highly acidic and stagnant micro-environment. Crevice corrosion initiates when the pH and chloride ions in the crevice solution disrupt the passivation layer. At this point, the rate of anodic reactions increases, further lowering the pH of the crevice solution while elevating the influx of anions into the crevice. Consequently, the metal deteriorates rapidly inside the crevice, leading to structural damage to the bulk alloy.

Evidence for crevice corrosion can be found in the crevice width-depth data (Figure 15). Overall, the widths of the corroded boundaries were 2-5 times larger than the depths. The non-CSL boundaries fell on the lower end of this range, while CSL boundaries typically had the larger width to depth ratios. As reflected in the EDS mapping data, the chromium depleted zones contained the area approximately 10-20 nm adjacent to the carbides, suggesting that the regions affected by sensitization were extremely localized. In CoCrMo alloys, grain boundary sensitization initiates a crevice of varying depths, depending on the density of carbides and the magnitude of Cr depletion.

Next, crevice corrosion initiated in these crevices, resulting in runaway corrosion. The crevices corroded laterally to a few microns and stopped as the anodic reactions inside the crevices were quenched. Chromium ions must come from the surface in order to proceed with crevice corrosion, yet if this reaction is quenched, the corrosion will stop.

Other crevice trends can also be used to explain other observations. As seen in the TEM im-

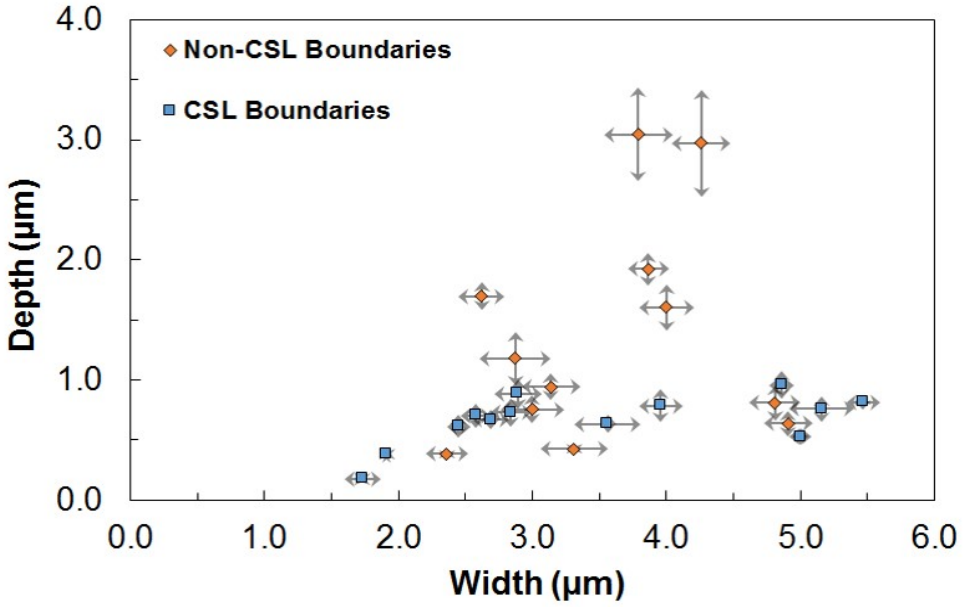

Figure 15: Depth and width measurements collected from 3D profilometry show that widths of the corroded grain boundaries are approximately 2-5 times larger than its corresponding depth. The arrows represent the range of measurements along the boundary.

ages, the carbides were irregularly spaced along the grain boundaries. With local grain boundary nucleation followed by crevice corrosion, there would be fluctuations in both the depth and width corrosion driving forces, depending on the local density of carbide precipitates. As confirmed in the depth-width data, almost all boundaries had large local fluctuations in the width and depth, represented by the arrows showing the ranges of each data point (Figure 15). Differences in carbide concentrations were observed for corroded CSLs and non-CSLs, with partially corroded CSLs containing smaller and fewer carbides. On the other hand, severely corroded CSL boundaries contained higher densities of larger carbides. Due to a larger density of carbides and larger Cr depletion, it is expected that non-CSL boundaries had a larger driving force down the boundary, resulting in bigger corrosion depths. Indeed, this was reflected in the width-depth data, as non-CSLs generally had lower width to depth ratios. Non-CSLs corroded down to 3 μm, with widths from 3-5 μm. CSL boundaries, on the contrary, only corroded to about 1 μm, with widths from 2-5 μm.

Profilometry clearly showed that the driving force due to sensitization had a lesser effect on

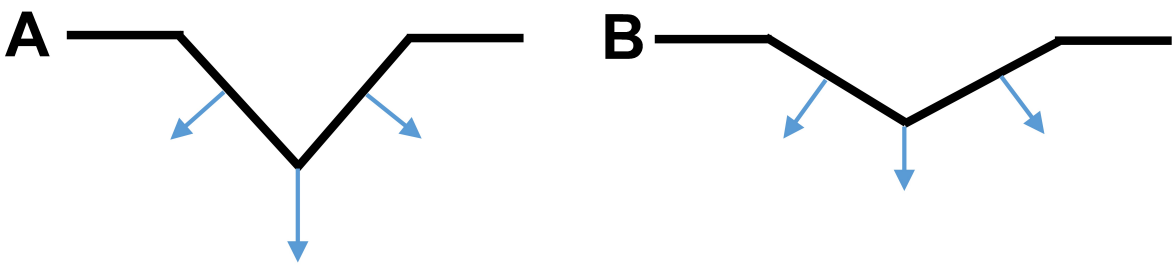

Figure 16: Schematic of the crevice cross-section illustrates that (A) non-CSL boundaries corroded more vertically as driving force due to sensitization is greater in comparison to (B) CSL boundaries.

CSL boundaries, as they had fewer and smaller carbides, which were characterized via nanoscale chemical analysis. By combining grain boundary sensitization and crevice corrosion, the depth and width driving forces for corrosion can be correlated to understand the corrosion behavior of CoCrMo grain boundaries, and the nanoscale experimental data can be effectively linked to the microscale observations.

4 Conclusions and Suggestions for Future Work

CoCrMo grain boundaries were studied in order to understand how different grain boundary properties impact the corrosion performance of the alloy. Coincidence site lattice geometry and chemical composition at the boundary were correlated to the localized corrosion properties. Using TEM and high-resolution EDS mapping, it was shown that higher magnitudes of chromium depletion and larger carbide precipitates scaled with increasing grain boundary interfacial energy. Additionally, it was also determined that there was a 2-6 at% of Cr depletion at CSL grain boundaries. The magnitude of chromium depletion was correlated with the geometry and interfacial energy of the boundary. The carbide precipitates ranged from 50-100 nm in length and 10-20 nm in width. 3D profilometry of the corroded surface morphology revealed that crevice corrosion had occurred at the crevices initiated by grain boundary sensitization. The crevice widths were 2-5 times larger than the crevice depths. Cr depletion provided a driving force for crevice initiation, which was observed from the crevice depth measurements. The anodic reactions inside the crevice, accompanied by a highly acidic micro-environent, provided the driving force for rapid metal dissolution. The crevices corroded laterally to a few microns and

stopped once the anodic reactions inside the crevices were quenched. Multiscale analysis of corroded CoCrMo grain boundaries showed that grain boundary sensitization initiated the attack and crevice corrosion then took over the dissolution process.

With new insights regarding how annealed CoCrMo alloys corroded, further processing modifications can be performed on these alloys for to achieve higher *in vivo* performance. Thermo-mechanical treatments, which combine annealing heat treatments with slight mechanical strains, can further increase the proportions of low-Σ CSL boundaries. By providing a slight compressive strain to the surface of CoCrMo alloys, CSL boundaries will become prevalent at the surface, while the bulk of the alloy will remain the same as before. This ensures that the top surface will be highly resistant to corrosion initiation, minimizing the onset of runaway crevice corrosion, and the alloy will still maintain its excellent mechanical properties. The microstructures resulting from these thermo-mechanical treatments and the corrosion performance of the treated CoCrMo alloys will need to be extensively studied before these new processing methods can be applied to future biomaterials.

Finally, computational studies to calculate the grain boundary interfacial energies of CoCrMo CSL boundaries would be desirable. With these energy values, minimal threshold values for the density of CSLs can be used to determine whether the CoCrMo alloy will corrode. This knowledge can further clarify the processing modifications required in order to manufacture high performance alloys. As a result, the engineering and design of new and more corrosion resistant CoCrMo alloys would be attainable.

5 References

1. M. L. Wolford, K. Palso, A. Bercovitz, Hospitalization for total hip replacement among inpatients aged 45 and over: United States, 2000-2010. NCHS Data Brief, 1-8 (2015).

2. B. Bashinskaya, R. M. Zimmerman, B. P. Walcott, V. Antoci, Arthroplasty Utilization in the United States is Predicted by Age-Specific Population Groups. ISRN Orthop 2012, 8 (2012).

3. I. Catelas, M. A. Wimmer, S. Utzschneider, Polyethylene and metal wear particles: characteristics and biological effects. Semin Immunopathol 33, 257-271 (2011).

4. S. A. Jacobsson, K. Djerf, O. Wahlstrom, 20-year results of McKee-Farrar versus Charnley prosthesis. Clinical Orthopaedics and Related Research, S60-S68 (1996).

5. S. Pramanik, A. K. Agarwal, K. N. Rai, Chronology of Total Hip Joint Replacement and Materials Development. Trends Biomater Artif Organs 19, 15-26 (2005).

6. L. D. Dorr, Z. I. Wang, D. B. Longjohn, B. Dubois, R. Murken, Total hip arthroplasty with use of the metasul metal-on-metal articulation - Four to seven-year results. Journal of Bone and Joint Surgery-American Volume 82A, 789-798 (2000).

7. C. P. Delaunay, F. Bonnomet, P. Clavert, P. Laffargue, H. Migaud, THA using metal-on-metal articulation in active patients younger than 50 years. Clin Orthop Relat Res 466, 340-346 (2008).

8. M. A. Wimmer, J. Loos, R. Nassutt, M. Heitkemper, A. Fischer, The acting wear mechanisms on metal-on-metal hip joint bearings: in vitro results. Wear 250, 129-139 (2001).

9. R. M. Urban et al., Dissemination of wear particles to the liver, spleen, and abdominal lymph nodes of patients with hip or knee replacement. J Bone Joint Surg Am 82, 457-476 (2000).

10. J. R. Scully, Environment-assisted intergranular cracking. MRS Bulletin 24, 36-42 (1999).

11. O. P. Arora, M. Metzger, Corrosion of Some Tilt and Twist Boundaries in Aluminum Bicrystals. Transactions of the Metallurgical Society of Aime 236, 1205 (1966).

12. G. Hasson, Herbeuva.I, J. Y. Boos, M. Biscondi, C. Goux, Theoretical and Experimental Determinations of Grain-Boundary Structures and Energies - Correlation with Various Experimental Results. Surface Science 31, 115 (1972).

13. D. Sun, J. A. Wharton, R. J. K. Wood, L. Ma, W. M. Rainforth, Microabrasion-corrosion of cast CoCrMo alloy in simulated body fluids. Tribology International 42, 99-110 (2009).

14. M. D. Sangid, H. Sehitoglu, H. J. Maier, T. Niendorf, Grain boundary characterization and energetics of superalloys. Materials Science and Engineering a-Structural Materials Properties Microstructure and Processing 527, 7115-7125 (2010).

15. P. Lin, G. Palumbo, U. Erb, K. T. Aust, Influence of Grain-Boundary-Character-Distribution on Sensitization and Intergranular Corrosion of Alloy-600. Scripta Metallurgica Et Materialia 33, 1387-1392 (1995).
16. P. Panigrahi et al., Intergranular pitting corrosion of CoCrMo biomedical implant alloy. Journal of biomedical materials research. Part B, Applied biomaterials 102, 850-859 (2014).
17. E. C. Bain, R. H. Aborn, J. J. B. Rutherford, The Nature and Prevention of Intergranular Corrosion in Austenitic Stainless Steels. Trans Am Steel Treating Soc 21, 481-509 (1933).
18. S. M. Bruemmer, L. A. Charlot, Development of Grain-Boundary Chromium Depletion in Type-304 and Type-316 Stainless-Steels. Scripta Metallurgica 20, 1019-1024 (1986).
19. E. Bettini, T. Eriksson, M. Bostrom, C. Leygraf, J. S. Pan, Influence of metal carbides on dissolution behavior of biomedical CoCrMo alloy: SEM, TEM and AFM studies. Electrochimica Acta 56, 9413-9419 (2011).
20. Y. Liao et al., New insights into hard phases of CoCrMo metal-on-metal hip replacements. J Mech Behav Biomed Mater 12, 39-49 (2012).
21. T. Watanabe, S. I. Kimura, S. Karashima, The Effect of a Grain-Boundary Structural Transformation on Sliding in (1010)-Tilt Zinc Bicrystals. Philosophical Magazine A-Physics of Condensed Matter Structure Defects and Mechanical Properties 49, 845-864 (1984).
22. B. Alexandreanu, B. Capell, G. S. Was, Combined effect of special grain boundaries and grain boundary carbides on IGSCC of Ni-16Cr-9Fe-xC alloys. Materials Science and Engineering a-Structural Materials Properties Microstructure and Processing 300, 94-104 (2001).
23. M. Shimada, H. Kokawa, Z. J. Wang, Y. S. Sato, I. Karibe, Optimization of grain boundary character distribution for intergranular corrosion resistant 304 stainless steel by twin-induced grain boundary engineering. Acta Materialia 50, 2331-2341 (2002).
24. G. Palumbo, K. T. Aust, Structure-Dependence of Intergranular Corrosion in High-Purity Nickel. Acta Metallurgica Et Materialia 38, 2343-2352 (1990).
25. H. W. Liu, M. Gao, D. G. Harlow, R. P. Wei, Grain-Boundary Character, and Carbide Size and Spatial-Distribution in a Ternary Nickel-Alloy. Scripta Metallurgica Et Materialia 32, 1807-1812 (1995).
26. A. Pardo et al., Influence of Ti, C and N concentration on the intergranular corrosion behaviour of AISI 316Ti and 321 stainless steels. Acta Materialia 55, 2239-2251 (2007).
27. R. Leiva-Garcia, M. J. Munoz-Portero, J. Garcia-Anton, Evaluation of Alloy 146, 279, 900, and 926 sensitization to intergranular corrosion by means of electrochemical methods and image

analysis. Corrosion Science 51, 2080-2091 (2009).
28. D. H. Warrington, P. Bufalini, Coincidence Site Lattice and Grain Boundaries. Scripta Metallurgica 5, 771 (1971).
29. D. G. Brandon, Structure of High-Angle Grain Boundaries. Acta Metallurgica 14, 1479 (1966).
30. M. Yamashita, T. Mimaki, S. Hashimoto, S. Miura, Intergranular Corrosion of Copper and Alpha-Cu-Al Alloy Bicrystals. Philosophical Magazine A-Physics of Condensed Matter Structure Defects and Mechanical Properties 63, 695-705 (1991).
31. V. Y. Gertsman, S. M. Bruemmer, Study of grain boundary character along intergranular stress corrosion crack paths in austenitic alloys. Acta Materialia 49, 1589-1598 (2001).
32. G. Palumbo, K. T. Aust, E. M. Lehockey, U. Erb, P. Lin, On a more restrictive geometric criterion for "special" CSL grain boundaries. Scripta Materialia 38, 1685-1690 (1998).
33. V. Randle, The coincidence site lattice and the 'sigma enigma'. Materials Characterization 47, 411-416 (2001).
34. R. Pareja, J. Serna, Failure of the Coincidence Site Lattice Model for Grain-Boundaries in Metallic Systems. Scripta Metallurgica 13, 99-101 (1979).
35. P. R. M. van Beers, V. G. Kouznetsova, M. G. D. Geers, M. A. Tschopp, D. L. McDowell, A multiscale model of grain boundary structure and energy: From atomistics to a continuum description. Acta Materialia 82, 513-529 (2015).
36. K. Sangwal, Etching of Crystals: Theory, experiment and applications. (Elsevier, 2012).